This is the peer-reviewed, final accepted version for American Mineralogist, published by the Mineralogical Society of America.
The published version is subject to change. Cite as Authors (Year) Title. American Mineralogist, in press.
DOI: https://doi.org/10.2138/am-2024-9289. http://www.minsocam.org/

Manuscript 9289R (Revision 1)

Word count: *6313*

Crystallographic insights into monovalent thallium incorporation: Exploring hydropyrochlore structure for environmental remediation

Alice Taddei[1], Luca Bindi[1], Giovanni O. Lepore[1], Henrik Skogby[2], Paola Bonazzi[1,*]

[1]Dipartimento di Scienze della Terra, Università degli Studi di Firenze, via La Pira 4, I-50121 Firenze, Italy

[2]Department of Geosciences, Swedish Museum of Natural History, Box 50007, SE-10405 Stockholm, Sweden

*paola.bonazzi@unifi.it

Abstract

Hydropyrochlore, ideally $(H_2O,\square)_2Nb_2(O,OH)_6(H_2O)$, is a cubic mineral (space group $Fd\bar{3}m$, a = 10.56-10.59 Å, Z = 8) belonging to the pyrochlore supergroup (general formula: $A_{2-m}B_2X_{6-w}Y_{1-n}$). The K-rich variety of this species is unique to the Lueshe syenitic-carbonatitic deposit (D.R. Congo), where it occurs as the alteration product of primary $(Ca,Na)_2Nb_2O_6F$ pyrochlores. The structure of this mineral is made of a B_2X_6 (B = Nb, Ti; X = O, OH) framework that generates tunnels along the

This is the peer-reviewed, final accepted version for American Mineralogist, published by the Mineralogical Society of America.
The published version is subject to change. Cite as Authors (Year) Title. American Mineralogist, in press.
DOI: https://doi.org/10.2138/am-2024-9289. http://www.minsocam.org/

[110] direction, where the interstitial sites are partially occupied by water molecules and minor amounts of different cations. These features form the basis for the ion-exchange properties of hydropyrochlore, making it a promising candidate as a mineral sink for heavy metals (e.g., Tl^{+}) dispersed in aqueous matrices, with interesting environmental implications.

Tl^{+} incorporation was induced through imbibition experiments in a diluted Clerici solution using single crystals of hydropyrochlore from Lueshe (D.R. Congo); the modifications induced by Tl^{+} incorporation were then evaluated through single-crystal X-ray diffraction (SCXRD), electron microprobe analyses (EMPA) and Fourier transform infrared (FT-IR) spectroscopy.

After Tl^{+} imbibition, a dramatic increase of the A-site electron density (n.e^{-} from ~4 to ~60) confirms the entry of a substantial amount of Tl^{+} at this site (up to about 70%), leading to a lengthening of the A-X distances and the consequent expansion of the unit cell. A decrease of the site scattering at the Y′ site (from ~9 to ~4 e^{-}) also occurs, suggesting a loss of aqueous species. Although the predominance of neutral H_2O molecules at the interstitial sites of hydropyrochlore from Lueshe is widely accepted by the mineralogical community, our crystal-chemical and FT-IR data provide evidence that the dominant species might be the hydronium ion, with significant implications on the nomenclature of the pyrochlore supergroup.

Understanding the crystallographic aspects of hydropyrochlore as a potential waste form for monovalent thallium immobilization not only addresses a pressing environmental concern, but also contributes to the broader field of waste management.

Keywords: hydropyrochlore; hydrokenopyrochlore; thallium; ion exchange; single-crystal X-ray diffraction; electron microprobe analysis; Fourier transform infrared spectroscopy.

Introduction

Pyrochlore minerals and their synthetic analogues have been extensively studied in the past decades, both for their complex chemistry and for their wide range of applications in various scientific and technological fields, thanks to their magnetic, dielectric, electrical, photocatalytic, and ion-exchange properties (Fukina et al. 2023 and references therein). In particular, the capability to incorporate large, toxic cations such as Tl^{+} dispersed in aqueous matrices is interesting from an environmental perspective.

The pyrochlore structure is distinctive in that it can host numerous cations and anions with different size and charge, favoring easy ion-exchange reactions. The general formula is $A_{2-m}B_2X_{6-w}Y_{1-n}$ [where A = Na^{+}, Ca^{2+}, K^{+}, Sr^{2+}, Ce^{3+}, U^{4+}, H_2O, etc.; B = Nb^{5+}, Ta^{5+}, Ti^{4+}, W^{6+}, Sb^{5+}, etc.; X = O^{2-}, $(OH)^{-}$; Y = $(OH)^{-}$, F^{-}, O^{2-}, H_2O, K^{+}]. The structure can be described as a framework of BX_6 octahedra that forms tunnels along [110] hosting the interstitial A and Y sites (e.g., Subramanian et al. 1983). When the Y site is occupied by large cations (i.e., K, Tl^{+}, Rb, Cs) and the A position is completely vacant, the structure type is known as *inverse pyrochlore* (Ercit et al. 1993).

Ion-exchange processes may take place at the interstitial sites located within the tunnels, especially when they are occupied by highly mobile species (such as H_2O) or when they are partially vacant, which is a common feature for natural, strongly weathered pyrochlores (e.g., hydropyrochlore; Ercit et al. 1994; Lumpkin and Ewing 1995, and hydrokenopyrochlore; Biagioni et al. 2018).

A variety of materials with the pyrochlore structure have been examined for applications in the environmental field because of their capability to immobilize toxic elements such as Pb or Sb (Han et al. 2014; Jurkovič et al. 2019; Park et al. 2021) or, more commonly, actinides and other hazardous radionuclides (Koivula et al. 2002; Ewing et al. 2004; McMaster et al. 2018). Although some authors have previously reported that monovalent thallium can be incorporated in natural, hydrated, defective pyrochlores by soaking them in Tl-rich solutions (Jäger et al. 1959; van der Veen 1963; Harris 1965; Bindi et al. 2006), there are few studies on their potential use as sinks for Tl^{+} (Zoppi 2004). It is thus crucial to further pursue the issue, since pollution from thallium is rapidly becoming a concerning

matter due to its high toxicity and enhanced mobility in aqueous solutions, especially when it is present in its reduced state (e.g., Biagioni et al. 2017). Numerous methods for Tl removal from wastewater have been developed in the recent years, including the exploitation of adsorption and ion-exchange properties of various materials (Xu et al. 2019; Zhao et al. 2020), but most of them have shown greatly reduced uptake efficiency in the presence of competitors such as H^+, Na^+, K^+, and Ca^{2+}. It is therefore worth to investigate the potential suitability of pyrochlores for the same application. The pyrochlore species that are most likely suitable for this purpose are those characterized by remarkable amounts of vacancies and/or leachable cations or water molecules at the A and Y sites.

In the present study, following preliminary indications obtained by Zoppi (2004), experiments were carried out on hydropyrochlore from Lueshe (Bwito, Rutshuru Territory, North Kivu, D.R. Congo), ideally $(H_2O,\square)_2Nb_2(O,OH)_6(H_2O)$. This mineral was firstly described by van Wambeke (1978) as *kalipyrochlore* (hydropyrochlore, following the current nomenclature; Atencio et al. 2010; Atencio 2021) and fully characterized by Ercit et al. (1994), who pointed out the partially inverse character of this structure and provided insights into the role of water in the tunnels.

At Lueshe, (Sr,K)-bearing hydropyrochlore occurs as a secondary product of primary $(Ca,Na)_2Nb_2O_6(OH,F)$ pyrochlores within the lateritic soils overlapping a syenite-carbonatite complex associated with secondary phosphates of the crandallite-goyazite series, Fe-Ti oxides and clays (Wall et al. 1996; Nasraoui and Bilal 2000). In the deposit, the supergene alteration causes chemical modifications involving a major leaching of the A cations and Y anions, the formation of structural vacancies, the incorporation of minor quantities of K^+, Sr^{2+}, Ba^{2+}, Ce^{3+}, and hydration (Lumpkin and Ewing 1995; Nasraoui and Bilal 2000).

Experimental methods

This is the peer-reviewed, final accepted version for American Mineralogist, published by the Mineralogical Society of America.
The published version is subject to change. Cite as Authors (Year) Title. American Mineralogist, in press.
DOI: https://doi.org/10.2138/am-2024-9289. http://www.minsocam.org/

From a large hydropyrochlore octahedral fragment, several single crystals (labelled L#) were extracted for single-crystal and powder X-ray diffraction (SCXRD, PXRD) investigations, electron microprobe analyses (EMPA) and imbibition experiments in a thallium-bearing solution (Tl-Imb), followed by desorption tests in deionized water (H_2O-Imb). The uptake/release mechanisms were also investigated through Fourier transform infrared spectroscopy (FT-IR).

Chemical analyses

Chemical analyses were carried out by means of a JEOL JXA-8230 electron microprobe, operated at 10 nA and 15 kV, on crystals L1, L11, L14 and L9_Tl after Tl-Imb, as well as some grains not characterized by X-ray diffraction. Counting times were 30 s (Fe, Pb, Ca, Sb, Ba, U, Na, F), 20 s (Ti, Sr), 15 s (K, Tl, Ce, La), and 10 s (Nb, Ta). Standards employed were albite (Na$K\alpha$), sanidine (K$K\alpha$), diopside (Ca$K\alpha$), ilmenite (Ti$K\alpha$ and Fe$K\alpha$), celestine (Sr$L\alpha$), Nb-metal (Nb$L\alpha$), barite (Ba$L\alpha$), monazite (Ce$L\alpha$ and La$L\alpha$), lorandite (Tl$M\alpha$), crocoite (Pb$M\alpha$), and U-metal (U$M\alpha$). ZAF correction was applied for absorption and matrix effects.

An overlap correction factor was calculated and applied to take into account the interference between Tl$M\alpha$ and Nb$L\alpha$. Given this interference issue, thallium values were measured again by increasing the voltage to 20 kV; no variations were observed.

F (fluorite; F$K\alpha$), Si (albite; Si$K\alpha$), Sb (Sb-metal; Sb$L\alpha$) and Ta (Ta-metal; Ta$M\alpha$) were sought but found below the detection limits (0.01-0.02 wt%). In order to check for the possible presence of NH_4^+, the λ range (3.0000-3.3214 nm) was scanned but no peak ascribable to N was observed.

Chemical data were normalized on the basis of ΣB cations = 2 with all the iron considered to be trivalent. Average values are reported in Table 1. Low EMPA analytical totals indicate the presence of significant amounts of H_2O (see below).

Single-crystal X-ray diffraction

This is the peer-reviewed, final accepted version for American Mineralogist, published by the Mineralogical Society of America.
The published version is subject to change. Cite as Authors (Year) Title. American Mineralogist, in press.
DOI: https://doi.org/10.2138/am-2024-9289. http://www.minsocam.org/

Unit-cell parameters and intensity data were collected using a Bruker D8 Venture diffractometer equipped with a Photon III detector, using graphite-monochromatized Mo*K*α radiation (λ = 0.71073 Å), before and after each imbibition experiment (Table 2). Intensity data were corrected for Lorentz-polarization effects and for absorption with *APEX2* (Bruker 2016).

Imbibition experiments

Five selected crystals (L7, L8, L9, L12, L19) were soaked for five days in a 1:1 H_2O-diluted Clerici solution. For L8_Tl an additional Tl-Imb was performed for three days (L8_2Tl). L8_2Tl and L19_Tl were subsequently soaked in deionized water for seven days (L8_2Tl-W and L19_Tl-W). A further water imbibition led to a major fracturing of L8_2Tl-2W into several domains.

Powder X-ray diffraction

In order to check the purity of the sample for the FT-IR investigations, about 4 mg of material were crushed in an agate mortar and the resulting powder was analyzed with a PANalytical X'Pert PRO diffractometer using Cu*K*α radiation (2θ range = 5-70°, step size = 0.017°, scan step time = 114.3 s). The powdered material was found to consist mainly of hydropyrochlore with minor amounts of ilmenite, a member of the crandallite-goyazite series, and likely very minor magnesian calcite.

FT-IR spectroscopy

Spectroscopic analyses were carried out using a Bruker Vertex 70 attached to a Hyperion 2000 microscope and equipped with a glowbar source, KBr beamsplitter and an MCT detector. IR spectra were acquired in transmission mode by placing the sample on a KBr plate and adjusting the aperture size to that of the sample. Measures were obtained from L19_Tl, L19_Tl-W and from small fragments of untreated sample (50-100 μm). The acquired IR spectra represent an average of 64 scans, with a spectral range between 6000 and 600 cm^{-1} and a resolution of 4 cm^{-1}. Additional measurements on untreated sample were taken using the KBr pellet method, by mixing 2 mg of the mineral with 200 mg of KBr in an agate mortar and then pressing the mixture to 12 mm diameter disc under a load of 4.5 tonnes.

Structural Refinements

Structural refinements were carried out in the space group $Fd\bar{3}m$ using SHELXL (Sheldrick 2015), setting the origin at $\bar{3}m$ (origin choice 2), which involves the A site at the Wyckoff position 16*d* (½, ½, ½), the B site at 16*c* (0, 0, 0), Y site at 8*b* (⅜, ⅜, ⅜) and X site at 48*f* (*x*, ⅛, ⅛). The *x*(48*f*) coordinate was refined starting from the value reported by Ercit et al. (1994). The Nb/Ti ratio was fixed at the averaged EMPA value, and the X site was assumed to be fully occupied by O. Convergence was achieved adopting an anisotropic model. With these sites alone, the atomic displacement parameter of the Y site, invariably extremely large, suggested intense positional disorder. A careful analysis of the ΔF map revealed the presence of a peak analogous to the ϕ″ site observed by Ercit et al. (1994). This peak corresponds to a partially occupied site here named Y′. The replacement of Y (8*b*) with Y′ (32*e*) led to an improvement of the overall refinement. In both untreated and H_2O-Imb crystals an additional A′ peak (32*e*) in the vicinity of the A site was observed. However, first attempts to model the positional disorder of the tunnel sites (A, A′, Y′) without constraints still led to rather high displacement parameters along with a strong correlation with their occupancy factors. Thus, following the procedure of Ercit et al. (1994), some constraints were applied based on the following assumptions: *i)* the A site was considered to be occupied by (Sr+Na+Ca+Pb) only, and its occupancy factor was fixed accordingly; *ii*) the occupancy of A′ was refined, and its atomic displacement parameter was constrained to be equal to that of the A site; *iii*) it was assumed that all K^+ is located at Y′ along with the aqueous species to complete ¼ of the 32*e* position occupancy. When available, the cationic content was taken from EMPA data; in the other cases, given the low variability of the chemical composition among the selected crystals, the chemical constraints were assigned considering the overall averaged values (Table 1). All atoms but B and X were refined isotropically. For H_2O-Imb treated crystal (L8_2Tl-W), the same constraints were applied, but the occupancies of

This is the peer-reviewed, final accepted version for American Mineralogist, published by the Mineralogical Society of America.
The published version is subject to change. Cite as Authors (Year) Title. American Mineralogist, in press.
DOI: https://doi.org/10.2138/am-2024-9289. http://www.minsocam.org/

the A and Y′ sites were refined. For Tl-Imb treated crystals, where A′ is no longer observed, it was possible to model the A site using anisotropic displacement parameters. The occupancy of both A and Y′ sites was refined leading to a satisfactory match between the number of electrons obtained by the refinement (A = 56.8, Y′ = 4.6) and that calculated on the basis of chemical composition (A = 55.5, Y′ = 3.8, see L9_Tl crystal in Table 1). The X site was refined using isotropic displacement parameters only for the L8_2Tl refinement.

Scattering curves for neutral atoms, taken from the *International Tables for Crystallography* (Wilson 1992), were used as follows: A = Sr vs. □ (untreated crystals) or Tl vs. □ (Tl-Imb and H_2O-Imb); A′ = O vs. □ (untreated crystals) or Tl vs. □ (H_2O-Imb); B = Nb vs. Ti; X = O; Y′ = K vs. O (untreated crystals) or K vs. □ (Tl-Imb and H_2O-Imb). Details of the data collections and structure refinements (Table 2) as well as bond distances and structural parameters (Table 3) are given for a selected set of crystals. Data related to the other crystals are given as supplementary material.

Results and Discussion

The crystal structure of hydropyrochlore from Lueshe here studied is topologically identical to that of cubic ($Fd\bar{3}m$) pyrochlores having a partially inverse character, and in particular it is rather similar to the one described by Ercit et al. (1994) for a sample from the same locality. Figure 1 shows the B_2X_6 framework of corner-linked octahedra forming tunnels along [110], wherein the A, A′ and Y′ sites are located.

Before imbibition all the tested crystals yielded a unit-cell parameter *a* ranging from 10.536 to 10.585 Å (Table 2), a range of values consistent with previous literature (van Wambeke 1978; Ercit et al. 1994). Following Tl^+ imbibition, the first structural evidence of the Tl^+ uptake is an expansion of the unit-cell parameter (*a* = 10.644-10.672 Å; Fig. 2) toward the value of 10.6829 Å measured for the

synthetic $Tl^{+}_{2-x}Tl^{3+}_{x}Nb_2O_{6+x}$ (x = 0.07) pyrochlore (Fourquet et al. 1995). Accordingly, EMPA data obtained after Tl^{+} imbibition showed a high Tl content accompanied by a high analytical total (99.06 wt%; Table 1), suggesting a substantial dehydration consequent to Tl^{+} incorporation.

The A site is located in the center of the tunnels, exhibiting a trigonal scalenohedral coordination determined by six oxygen atoms at X and other two at Y′, when the latter is occupied by aqueous species. In hydropyrochlore from Lueshe, A is dominated by structural vacancies with a mixed (Sr, Na, Ca, Pb^{2+}) cationic population ranging from 0.20 to 0.36 apfu. Sr is the most abundant cation and shows similar values in each measured grain (0.17-0.18 apfu), constantly higher than those reported in the literature (van Wambeke 1978; Ercit et al. 1994). On the other hand, given its high leachability, the Na content is rather variable (0.01-0.17 apfu). Minor amounts of Ca (0.01 apfu) and Pb^{2+} (up to 0.01 apfu) are also observed. After Tl^{+} imbibition, a dramatic increase of the site scattering ($n.e^{-}$ from ~4 to ~60) indicates the entry of a conspicuous amount of Tl^{+} at the A site (up to about 70%), leading to a lengthening of the A-X distance (Table 3). After desorption experiments (L8_2Tl-W), a remarkable decrease of electrons at the A site (from 61.0 to 38.3) is observed, suggesting partial Tl^{+} loss. Nonetheless, the cell parameter decreases less than expected (Fig. 2). Further imbibition experiments in deionized water (L8_2Tl-2W) led to a fracturing of the crystal, preventing any further SCXRD investigation.

The additional A′ peak in the vicinity of the A site, present in untreated crystals, is no longer observed after Tl^{+} imbibition. Interestingly, it occurs again after the final treatment in water thus corroborating the hypothesis that A′ hosts mainly an aqueous species even if the presence of a minor amount of Tl^{+} at this site in the water-imbibed crystal cannot be completely ruled out. Given the high positional disorder of A and A′, atomic displacement parameters are strongly correlated with the site scattering. The disappearance of A′ could then be related to the increase of the electrons number at the A site, which is in turn associated with an almost quadruple atomic displacement parameter (see CIFs

deposited). Thus, this could explain either why A′ is not observed after Tl^+ imbibition and the new appearance of the extra site after the treatment in water.

As shown by chemical data, the B site exhibits a quite constant composition, with Nb as the main constituent (1.83-1.86 apfu) partially replaced by Ti (0.14-0.17 apfu). Such a limited chemical variation well reflects the very narrow range of the B-X octahedral distances, either before (1.979-1.989 Å) and after (1.988-1.995 Å) the imbibition experiments. Although the B octahedron is not directly involved in the accommodation of Tl^+, it is affected by some geometrical variations, since it shares an edge with the A polyhedron. When the large Tl^+ cation induces an increase of the <A-X> distance, the shared X-X edge lengthens, becoming longer than the unshared one (Fig. 3). Consequently, the B octahedron, extremely regular ($<\sigma^2> = 0.12$) before the Tl^+ incorporation at A, slightly stretches along the 3-fold axis ($<\sigma^2> = 0.70$; Table 3). In principle, if A is occupied by a relatively highly charged, small cation (e.g., Ce^{3+} or Ce^{4+}), the shared edge should shorten, and the octahedron should exhibit a slight flattening along its 3-fold axis.

The Y′ site, in untreated crystals, is assumed as completely occupied by aqueous species and K. Such an assignment is based on the hypothesis that the cation hosted at Y′, if any, should be the largest one (Ercit et al. 1993), thus implying a certain degree of inversion already inferred by Ercit et al. (1994) for hydropyrochlore from Lueshe. The coordination sphere around Y′ when it hosts K is achieved by six oxygen atoms at X (Table 3) and, if water occupies the A′ site, by two additional oxygen atoms ($^{Y'}K$-$^{A'}O$ distance from 2.68 to 2.86 Å). Noteworthy, the Y′-A distance is far too short to justify a cation-cation separation: consequently, when Y′ is occupied by K, the A site must be vacant. The number of vacancies at A calculated for all the X-rayed crystals satisfies this requirement rather well, taking into consideration the uncertainty of the indirect determination method, especially in the presence of heavy elements (Table 1). Constraints also exist when Y′ is occupied by aqueous species: the site is surrounded by eight partially occupied A′ sites, but only three A′-Y′ distances are suitable for O···O separations. Moreover, the occupancy of A′ is also prevented by the occurrence of cations

This is the peer-reviewed, final accepted version for American Mineralogist, published by the Mineralogical Society of America.
The published version is subject to change. Cite as Authors (Year) Title. American Mineralogist, in press.
DOI: https://doi.org/10.2138/am-2024-9289. http://www.minsocam.org/

at A. Thus, even in the case of a completely empty A site, the maximum amount of H_2O at the A′ site cannot exceed 3/8, and the maximum total amount of H_2O pfu can be described as follows: $H_2O_{max} = {}^{Y'}1 + 3/8{}^{A}\square$, where ${}^{A}\square$ represents the vacancies (pfu) at A (Ercit et al. 1994). Such a configuration allows O···O bridges between oxygen atoms belonging to aqueous species (${}^{A'}O$-${}^{Y'}O$ in the range 2.68-2.86 Å).

After the incorporation of thallium, the number of electrons at the Y′ site decreases to about half of that in untreated crystals. At this point, Y′ should be predominantly vacant, hosting most of the initial K together with very minor Tl^+, as deduced from a comparison between the refined site scattering and the EMPA data. Indeed, the large amount of Tl^+ incorporated at A requires a vacancy-dominated Y′ site, because of the above discussed stereochemical reasons (A-Y′ distance ranging from 2.51 to 2.58 Å). In particular, Y′, which can be occupied up to ¼ (= 1 pfu) if A is completely vacant, must have additional vacancies at least equal to 1/32 (= 1/8 pfu) of the sum of the A cations pfu (${}^{Y'}\square \geq ¾ + \Sigma_{Acat.}/8$). This is verified also for L9_Tl, within the experimental uncertainty (Table 1).

The entry of the above-described amounts of Tl^+ requires necessarily a loss of positive charge to achieve charge neutrality. The cations that could potentially exchange with Tl^+, in particular Sr^{2+} and K^+, are not enough and tend to be retained in the structure after Tl^+ incorporation (Table 1). Thus, charge neutrality must be achieved mainly by H^+ loss. To account for the site scattering decrease at the Y′ and A′ sites, as well as the high analytical total after Tl^+ imbibition, the following two balancing mechanisms are plausible:

$$ {}^{A}\square + {}^{A'+Y'}H_2O + {}^{X}OH^- \rightleftarrows {}^{A}Tl^+ + {}^{A'+Y'}\square + {}^{X}O^{2-} \quad (1) $$

$$ {}^{A}\square + {}^{A'+Y'}H_3O^+ + {}^{X}O^{2-} \rightleftarrows {}^{A}Tl^+ + {}^{A'+Y'}\square + {}^{X}O^{2-} \quad (2) $$

In the hypothesis that the aqueous species at A′ and Y′ before Tl^+ incorporation is represented by water molecules, a dehydrogenation should occur at the anionic X site (1) concurrently with the entry

of Tl^+. As shown in Table 4, the two mechanisms lead to formulae with different degrees of $OH^- \rightarrow O^{2-}$ substitution at X, even before Tl^+ incorporation. In the hypothesis that the untreated mineral contains H_2O [mechanism (1)], a very large amount of OH^- should replace O^{2-} at the X site, which should thus show a very low bond-valence sum if the contribution of the covalent O-H bond is neglected. The bond-valence sums on the X site [parameters from Brese and O'Keeffe (1991) and Ferraris and Ivaldi (1988)] were calculated on the basis of the formulae derived from both mechanism (1) and (2) (Table 4, Fig. 4). In both cases, the obtained values (1.84/1.93, 1.86/1.98, 1.88/2.00 valence units for L1, L11 and L14 respectively) are hardly compatible with the large extent of hydrogenation at the X site required by the balancing mechanism (1). This constitutes an indirect proof of the presence of H_3O^+ in the structure.

It can be noted that in L1 and L14 crystals (Table 4) the structural vacancies rather than the aqueous species are dominant at (A + A′). Therefore, on the basis of the current nomenclature system (Atencio et al. 2010; Atencio 2021), they are to be referred to as hydrokenopyrochlore [ideal formula $(□,\#)_2Nb_2O_6 \cdot H_2O$ (Biagioni et al. 2018)].

The IR spectrum of untreated sample acquired with the KBr pellet method (Fig. 5a) is similar to that obtained by Nasraoui et al. (1999), yielding a large absorption band from 3600 to 3000 cm^{-1} in the O-H stretching zone. In particular, at least two peaks at 3400 and 3230 cm^{-1} due to O-H stretching in different crystal-chemical environments are observed. The H-O-H bending mode occurs at 1634 cm^{-1}. An additional peak at 1404 cm^{-1} in the spectrum could be assigned to C-O vibration modes, possibly due to relict carbonate minerals included in the studied sample. The two bands visible at 1035 and 883 cm^{-1} are due to the vibration modes of P-O bonds, confirming the presence of phosphates inclusions (crandallite-goyazite series). The band at 1035 cm^{-1} exhibits a shoulder at 960 cm^{-1}, that together with a very intense peak at around 650 cm^{-1} (out of scale in Figure 5a) can be attributed to the stretching vibrations of the octahedral bonds (Nb-O, Ti-O) (Geisler et al. 2004).

This is the peer-reviewed, final accepted version for American Mineralogist, published by the Mineralogical Society of America.
The published version is subject to change. Cite as Authors (Year) Title. American Mineralogist, in press.
DOI: https://doi.org/10.2138/am-2024-9289. http://www.minsocam.org/

The spectrum directly acquired from a minute fragment of untreated pyrochlore (Fig. 5b) shows a similar profile to that obtained from KBr pellet, but the intensities of the peaks are stronger, enough to make the band in the O-H stretching zone severely out of scale. However, there is a key difference between these spectra, namely the presence of an unusual peak at 1729 cm^{-1}. According to Chukanov (2014), an anomalous band in the range between 1700-1800 cm^{-1}, usually observed in the IR spectra of hydronium-bearing minerals, is interpreted as the υ4 bending mode of H_3O^+ [e.g., 1730 cm^{-1} in IR spectrum of larisaite, $Na(H_3O^+)(UO_2)_3(SeO_3)_2O_2{\cdot}4(H_2O)$, Chukanov et al. (2004); 1725 cm^{-1} in IR spectrum of chernikovite, $(H_3O^+)(UO_2)(PO_4){\cdot}4(H_2O)$, Armstrong and Clark (2010)]. It is important to remark that none of the minerals associated with hydropyrochlore from Lueshe exhibits a peak close to that observed at 1729 cm^{-1}. On the other hand, the signal ascribable to other vibrational modes of the hydronium ion (υ1 = 3160 cm^{-1}; υ2 = 1050-1140 cm^{-1}; υ3 = 3320 cm^{-1}), in particular υ2, may be hidden by the presence of strong O-H bands and significant inclusions of phosphates and carbonates in the sample.

The IR spectrum of L19_Tl shows much less intense and broader bands corresponding to the O-H stretching (3550-3000 cm^{-1}) and the H-O-H bending mode (1641 cm^{-1}) (Fig. 5c), indicating a much lower water content, which can be estimated as roughly 5% of that originally present in the untreated sample, in good agreement with the crystal-chemical formula obtained for the L9_Tl crystal (Table 4), which requires H_2O = 0.70 wt% whereas in the untreated crystals the calculated H_2O ranges from 12.43 to 14.19 wt%. Noteworthy, the peak at 1729 cm^{-1} is no longer observed in the spectrum of the Tl^+-rich crystal, suggesting loss of H_3O^+ in favour of Tl^+.

Imbibition experiments in deionized water cause an increase in intensity of the bands ascribed to the aqueous species (Fig. 5d), although it does not reach the values observed in untreated samples, in agreement with the entry of aqueous species (H_2O or H_3O^+) concomitant with Tl^+ partial loss. Interestingly, the peak at 3281 cm^{-1} in the O-H stretching zone is much sharper than the corresponding bands observed in the other spectra, possibly indicating a partial ordering of the molecules in the

tunnels of the pyrochlore structure. The occurrence of an additional peak at 1539 cm^{-1} remains unexplained.

Implications

Monovalent thallium is a highly toxic element that poses significant environmental and health risks due to its ability to accumulate in various ecosystems. The immobilization of monovalent thallium in polluted environments is a critical challenge, demanding effective waste forms capable of securely sequestering this hazardous metal ion. This study focused on the structural variations subsequent to imbibition experiments and unequivocally demonstrated that this cation is not merely adsorbed on the surface of the crystal, instead it enters the structure. In particular, the considerable structural changes observed are consistent with the entry of conspicuous amounts of Tl^+ at the A site (up to about 70%), leading to a significant increase of the volume of the A polyhedron, which in turn causes the expansion of the unit cell and minor adjustments in the edge-sharing B octahedron. Tl^+ incorporation appears strongly linked to the initial amount of aqueous species (namely hydronium ions) rather than the amount of structural vacancies (Fig. 6). Although the predominance of neutral H_2O molecules at the interstitial sites of hydropyrochlore from the Lueshe deposit is widely accepted by the mineralogical community, both FT-IR and crystal-chemical data here obtained provide evidence that the dominant species could actually be the hydronium ion, with significant implications also on the nomenclature of the pyrochlore supergroup. Nonetheless, the choice between H_2O or H_3O^+ is far from obvious. The presence of hydronium in minerals has been investigated with different spectroscopical methods (IR, Raman, ^1H and ^2H NMR, etc.) through the years, but the proof of its actual presence is, in many cases, weak or indirect (Ripmeester et al. 1986). Interestingly, neutron powder diffraction studies on antimonic acid having a pyrochlore-like structure demonstrated the

occurrence of interstitial hydronium ions (Slade et al. 1996; Alonso and Turrillas 2005), confirming that H_3O^+ can be actually hosted within the pyrochlore tunnels.

In summary, this study underlines the capabilities of the mineral from Lueshe to incorporate remarkable amounts of Tl^+, although there are still some open questions about the actual suitability of hydropyrochlore as a sink for thallium dispersed in polluted natural or industrial aqueous solutions. Worthy to note, imbibition in deionized water caused the loss of about one third of the total Tl^+ previously incorporated, thus it will still be necessary to investigate the effect of other parameters (i.e., pH of the solution, temperature, pressure) on the capability of the structure to retain the thallium incorporated as well as the influence of other variables (e.g., duration of the imbibition experiments, concentration of Tl^+ in the solutions, presence of competing cations in the solution, etc.) on the performance of the uptake/release process.

Acknowledgements

The authors acknowledge CRIST, Centro di Studi per la Cristallografia Strutturale, Università degli Studi di Firenze (Italy) and Naturhistoriska Riksmuseet, Stockholm (Sweden) for X-ray diffraction (single-crystal and powder, respectively) measurements. Electron microprobe analyses were carried out at LaMA, Laboratorio di MicroAnalisi, Università degli Studi di Firenze (Italy), and FT-IR spectra were collected at the Naturhistoriska Riksmuseet, Stockholm (Sweden). C. Ferraris (Muséum National d'Histoire Naturelle, Paris, France) and M. Batoni (private collector) are warmly thanked for providing the samples. The paper benefited from the useful suggestions and comments of the Associate Editor E.S. Grew, D. Atencio, and other two anonymous reviewers. This research received financial support by Università degli Studi di Firenze through the project BONAZZI_RICATEN23-Pyrochlore supergroup minerals: potential sinks for toxic elements in aqueous matrices, prot. 58517.

References

Alonso, J.A., and Turrillas, X. (2005) Location of H^+ sites in the fast proton-conductor $(H_3O)SbTeO_6$ pyrochlore. Dalton Transactions, 5, 865-867.

Armstrong, C.R., and Clark, S.B. (2010) Delineating hydrated uranyl phosphates: Powder XRD and ATR-IR studies. IOP Conference Series: Materials Science and Engineering, 9, 012040.

Atencio, D. (2021) Pyrochlore-supergroup minerals nomenclature: An update. Frontiers in Chemistry, 9, 713368.

Atencio, D., Andrade, M.B., Christy, A.G., Gieré, R., and Kartashov, P.M. (2010) The pyrochlore supergroup of minerals: nomenclature. Canadian Mineralogist, 48, 673-698.

Biagioni, C., D'Orazio, M., Lepore, G.O., D'Acapito, F., and Vezzoni, S. (2017) Thallium-rich rust scales in drinkable water distribution systems: A case study from northern Tuscany, Italy. Science of The Total Environment, 587-588, 491-501.

Biagioni, C., Meisser, N., Nestola, F., Pasero, M., Robyr, M., Roth, P., Schnyder, C., and Gieré, R. (2018) $(□,\#)_2Nb_2O_6·H_2O$, a new species of the pyrochlore supergroup from the Sahatany Pegmatite Field, Antananarivo Province, Madagascar. European Journal of Mineralogy, 30, 869-876.

Bindi, L., Petříček, V., Withers, R.L., Zoppi, M., and Bonazzi, P. (2006) A novel high-temperature commensurate superstructure in a natural bariopyrochlore: A structural study by means of a multiphase crystal structure refinement. Journal of Solid State Chemistry, 179, 729-738.

Brese, N.E., and O'Keeffe, M. (1991) Bond-valence parameters for solids. Acta Crystallographica, B47, 192-197.

Bruker (2016) APEX3, SAINT and SADABS. Bruker AXS Inc., Madison, Wisconsin, USA.

Chukanov, N.V. (2014) Infrared spectra of mineral species: Extended library, 1726 p., Springer Science and Business Media, Dordrecht, The Netherlands.

Chukanov, N.V., Pushcharovsky, D.Y., Pasero, M., Merlino, S., Barinova, A.V., Möckel, S., Pekov, I.V., Zadov, A.E., and Dubinchuk, V.T. (2004) Larisaite, $Na(H_3O)(UO_2)_3(SeO_3)_2O_2{\cdot}4H_2O$, a new uranyl selenite mineral from Repete mine, San Juan County, Utah, U.S.A. European Journal of Mineralogy, 16, 367-374.

Ercit, T.S., Černý, P., and Hawthorne, F.C. (1993) Cesstibtantite—a geologic introduction to the inverse pyrochlores. Mineralogy and Petrology, 48, 235-255.

Ercit, T.S., Hawthorne, F.C., and Černý, P. (1994) The structural chemistry of kalipyrochlore, a "hydropyrochlore". Canadian Mineralogist, 32, 415-420.

Ewing, R.C., Weber, W.J., and Lian, J. (2004) Nuclear waste disposal—pyrochlore ($A_2B_2O_7$): Nuclear waste form for the immobilization of plutonium and "minor" actinides. Journal of Applied Physics, 95, 5949-5971.

Ferraris, G., and Ivaldi, G. (1988) Bond valence vs bond length in O···O hydrogen bonds. Acta Crystallographica, B44, 341-344.

Fourquet, J.L., Duroy, H., and Lacorre, Ph. (1995) $Tl_2Nb_2O_{6+x}$ ($0 \leq x \leq 1$): A continuous cubic pyrochlore type solid solution. Journal of Solid State Chemistry, 114, 575-584.

Fukina, D.G., Belousov, A.S., and Suleimanov, E.V., Eds. (2023) Pyrochlore oxides: Structure, properties and potential in photocatalytic applications, 1st ed., 234 p. Springer Nature, Cham, Switzerland.

Geisler, T., Berndt, J., Meyer, H.W., Pollok, K., and Putnis, A. (2004) Low- temperature aqueous alteration of crystalline pyrochlore: correspondence between nature and experiment. Mineralogical Magazine, 68, 905-922.

Han, Y.N., Jiao, S., Xu, M., Pang, G., and Feng, S. (2014) Solvothermal synthesis of the defect pyrochlore $KNbWO_6{\cdot}H_2O$ and its application in Pb^{2+} removal. RSC Advances, 4, 14357-14360.

Harris, P.M. (1965) Pandaite from the Mrima Hill niobium deposit (Kenya). Mineralogical Magazine, 35, 277-290.

Jäger, E., Niggli, E., and van der Veen, A.H. (1959) A hydrated barium-strontium pyrochlore in a biotite rock from Panda Hill, Tanganyika. Mineralogical Magazine, 32, 10-25.

Jurkovič, L., Majzlan, J., Hiller, E., Klimko, T., Voleková-Lalinská, B., Méres, Š., Göttlicher, J., and Steininger, R. (2019) Natural attenuation of antimony and arsenic in soils at the abandoned Sb-deposit Poproč, Slovakia. Environmental Earth Sciences, 78, 672.

Koivula, R., Harjula, R., and Lehto, J. (2002) Structure and ion-exchange properties of tin antimonates with various Sn and Sb contents. Microporous and Mesoporous Materials, 55, 231-238.

Lumpkin, G.R., and Ewing, R.C. (1995) Geochemical alteration of pyrochlore group minerals: Pyrochlore subgroup. American Mineralogist, 80, 732-743.

McMaster, S.A., Ram, R., Faris, N., and Pownceby M.I. (2018) Radionuclide disposal using the pyrochlore supergroup of minerals as a host matrix—A review. Journal of Hazardous Materials, 360, 257-269.

Nasraoui, M., and Bilal, E. (2000) Pyrochlores from the Lueshe carbonatite complex (Democratic Republic of Congo): a geochemical record of different alteration stages. Journal of Asian Earth Sciences, 18, 237-251.

Nasraoui, M., Bilal, E., and Gibert, R. (1999) Fresh and weathered pyrochlore studies by Fourier transform infrared spectroscopy coupled with thermal analysis. Mineralogical Magazine, 63, 567-578.

Park., S.-C., Boyanov, M.I., Kemner, K.M., O'Loughlin, E.J., and Kwon, M.J. (2021) Distribution and speciation of Sb and toxic metal(loid)s near an antimony refinery and their effects on indigenous microorganisms. Journal of Hazardous Materials, 403, 123625.

Ripmeester, J.A., Ratcliffe, C.I., Dutrizac, J.E., and Lambor, J.L. (1986) Hydronium ion in the alunite-jarosite group. Canadian Mineralogist, 24, 453-447.

Robinson, K., Gibbs, G.V., and Ribbe, P.H. (1971) Quadratic elongation: a quantitative measure of distortion in coordination polyhedra. Science, 172, 567-570.

Sheldrick, G.M. (2015) Structure refinement with SHELXL. Acta Crystallographica, C71, 3-8.

Slade, R.C.T., Hall, G.P., Ramanan, A., and Prince, E. (1996) Structure and proton conduction in pyrochlore-type antimonic acid: a neutron diffraction study. Solid State Ionics, 92, 171-181.

Subramanian, M.A., Aravamudan, G., and Subba Rao, G.V. (1983) Oxide pyrochlores — A review. Progress in Solid State Chemistry, 15, 55-143.

van der Veen, A.H. (1963): A study of pyrochlore. Verhandelingen van het Koninklijk Nederlands geologisch mijnbouwkundig genootschap, Geologische serie, 22, 1-188.

van Wambeke, L. (1978) Kalipyrochlore, a new mineral of the pyrochlore group. American Mineralogist, 63, 528-530.

Wall, F., Williams, C.T., Woolley, A.R., and Nasraoui, M. (1996) Pyrochlore from weathered carbonatite at Lueshe, Zaire. Mineralogical Magazine, 60, 731-750.

Wilson, A.J.C. (1992) International Tables for Crystallography. Volume C: Mathematical, Physical and Chemical Tables. Kluwer Academic Publishers, Amsterdam.

Xu, H., Luo, Y., Wang, P., Zhu, J., Yang, Z., and Liu, Z. (2019) Removal of thallium in water/wastewater: A review. Water Research, 165, 114981.

Zhao, Z., Xiong, Y., Cheng, X., Hou, X., Yang, Y., Tian, Y., You, J., and Xu, L. (2020) Adsorptive removal of trace thallium(I) from wastewater: A review and new perspectives. Journal of Hazardous Materials, 393, 122378.

Zoppi, M. (2004) Ossidi di Nb, Ta e Ti: processi di ricristallizzazione e relazioni cristallochimiche, 166 p. Ph.D thesis, Università degli Studi di Firenze, Firenze (in Italian).

This is the peer-reviewed, final accepted version for American Mineralogist, published by the Mineralogical Society of America.
The published version is subject to change. Cite as Authors (Year) Title. American Mineralogist, in press.
DOI: https://doi.org/10.2138/am-2024-9289. http://www.minsocam.org/

Figure captions

Figure 1. Structural sketch of hydropyrochlore from Lueshe. The B_2X_6 octahedral framework forms pseudo-hexagonal tunnels that host the partially occupied A (black), A′ (red) and Y′ (yellow) sites. Projection approximately down the [110] axis.

Figure 2. Unit cell parameter plotted against the number of electrons at the A and A′ sites. Empty, filled and half-filled symbols represent untreated, Tl-Imb and H_2O-Imb crystals, respectively (* denotes the second imbibition in Tl^+-rich solution). Crystals that underwent imbibition experiments are colored as follows: L7 = red, L8 = orange, L9 = blue, L12 = green, L19 = purple. The black star symbol indicates $Tl^+_{2-x}Tl^{3+}_xNb_2O_{6+x}$ (x = 0.07) (Fourquet et al. 1995). Regression line (fitting the equation $y = 0.0018x + 10.550$, $r^2 = 0.91$) is calculated with samples only from this study.

Figure 3. Unshared- and shared-octahedral edges variation as function of the A-X distance [Δ(X-X) = (unsh. X-X – sh. X-X)/<X-X>]. Symbols as in Figure 2, except for L7 (= red empty circle) and L19 (= purple empty circle). In the synthetic $Tl^+_{2-x}Tl^{3+}_xNb_2O_{6+x}$ (x = 0.07) pyrochlore (<A-X> = 2.813 Å; Fourquet et al. 1995), not reported in figure, the difference between unshared and shared octahedral edges is even more pronounced [Δ(X-X) = –0.0661].

Figure 4. Sketch of the structural environment of the X site (view along [100]). The bond valence sum on the X site was calculated considering the contribution of two B sites, two A sites, one (½ + ½) A′ site and ¼ Y′ site (see text for explanation).

Figure 5. FT-IR spectra acquired from (**a**) KBr pellet containing untreated hydropyrochlore powder; (**b**) a small, untreated hydropyrochlore fragment. The weak bands in the range 4000-5100 cm^{-1} are attributable to water combination modes; (**c**) L19_Tl crystal; (**d**) L19_Tl-W crystal. Bands in the

range 2800-3000 cm^{-1} are due to C-H vibrational modes, possibly due to contamination from possible glue residues on the crystal.

Figure 6. Relation between the amount of Tl^{+} incorporated and the initial content of H_3O^{+} (or H_2O) at A′+Y′. Symbols as in Figure 2. Solid line (fitting the regression equation: $y = 0.5x + 0.7$, $r^2 = 0.82$) shows the rough correlation between the two parameters. The amount of initial H_2O or H_3O^{+} has been indirectly estimated from the number of electrons found at A′ and Y′. Analogously, the Tl^{+} values were tentatively derived from the refined site scattering at the A site and taking into account the Sr content as found by microprobe analysis (L9_Tl).

Table 1. Average microprobe analyses (wt% oxides) of untreated and treated crystals together with the crystal-chemical formulae on the basis of ΣB = 2.

	A	**B**	**C**	**D**	**E**	**L1**	**L11**	**L14**	**Range n.e$^-$**	**Mean**	**L9_Tl**
n	2	4	4	6	4	6	6	9			5
Nb_2O_5	77.53	74.46	75.86	74.12	75.14	74.42	74.03	73.03		74.82	43.21
TiO_2	4.00	3.59	3.49	3.97	3.80	4.18	3.84	3.93		3.85	2.38
Fe_2O_3	-	0.03	0.06	0.11	0.06	0.04	0.04	0.03		0.05	0.01
Na_2O	0.53	1.55	0.08	0.11	0.40	0.84	0.09	0.49		0.51	0.03
K_2O	1.18	1.74	1.42	1.59	1.24	1.51	1.53	1.28		1.44	0.51
CaO	0.13	0.15	0.11	0.24	0.10	0.09	0.11	0.12		0.13	0.03
SrO	5.55	5.46	5.49	5.44	5.57	5.83	5.65	5.56		5.57	3.14
Ce_2O_3	-	0.04	0.03	0.05	0.02	0.02	0.03	0.12		0.04	0.05
La_2O_3	-	0.05	-	0.04	0.04	-	-	0.01		0.02	-
UO_2	-	0.03	0.07	0.06	0.06	0.04	0.05	0.03		0.04	-
BaO	0.14	0.14	0.15	0.17	0.14	0.17	0.19	0.17		0.16	0.07
PbO	0.29	0.33	0.33	0.31	0.35	0.36	0.33	0.33		0.33	-
Tl_2O	-	-	-	-	-	-	-	-		-	49.63
Total	89.35	87.57	87.09	86.21	86.92	87.50	85.89	85.10		86.96	99.06
H_2O*						12.43	14.19	13.90			0.70
TOTAL						99.93	100.08	99.00			99.76
Nb^{5+}	1.84	1.85	1.86	1.83	1.85	1.83	1.84	1.84	75.0-76.3	1.84	1.83
Ti^{4+}	0.16	0.15	0.14	0.16	0.15	0.17	0.16	0.16	3.1-3.7	0.16	0.17
Fe^{3+}	-	-	-	0.01	-	-	-	-	0.0-0.3	-	-
Na^+	0.05	0.17	0.01	0.01	0.04	0.09	0.01	0.05	0.1-1.9	0.05	0.01
K^+	0.08	0.12	0.10	0.11	0.09	0.11	0.11	0.09	1.5-2.3	0.10	0.06
Ca^{2+}	0.01	0.01	0.01	0.01	0.01	0.01	0.01	0.01	0.2	0.01	-
Sr^{2+}	0.17	0.17	0.17	0.17	0.18	0.18	0.18	0.18	6.5-6.8	0.18	0.17
Ce^{3+}	-	-	-	-	-	-	-	-	-	-	-

La^{3+}	-	-	-	-	-	-	-	-	-	-	-
U^{4+}	-	-	-	-	-	-	-	-	-	-	-
Ba^{2+}	-	-	-	-	-	-	-	-	-	-	-
Pb^{2+}	-	0.01	0.01	0.01	0.01	0.01	0.01	0.01	0.0-0.8	0.01	-
Tl^{+}	-	-	-	-	-	-	-	-	-	-	1.32

Notes: *n* = number of analytical points; *H_2O calculated on the basis of the formulae reported in Table 4.

Table 2. SCXRD experimental details and crystal data for the selected crystals.

	L1	**L8**	**L8_2Tl**	**L8_2Tl-W**
a (Å)	10.555(2)	10.5567(8)	10.6444(8)	10.6397(6)
V (Å^3)	1175.7(5)	1176.5(3)	1206.0(3)	1204.4(2)
size (μm)	65×60×40	60×60×50	60×60×50	60×60×50
θ_{max} (Mo$K\alpha$)	32	32	32	32
R_{int} (%)	9.24	5.60	5.38	5.14
indep. refl.	125	124	129	129
obs. refl. $[F_o > 4\sigma(F_o)]$	97	108	103	105
Ref. param.	13	12	11	14
$R1_{all}$ (%)	4.85	3.33	4.74	5.32
$R1_{obs}$ (%)	3.28	2.74	3.74	3.99
$\Delta\rho_{max}$ (e/Å^3)	0.69	0.41	1.16	1.68
$\Delta\rho_{min}$ (e/Å^3)	–0.55	–0.79	–0.77	–0.96

	L9	**L9_Tl**	**L11**	**L14**
a (Å)	10.5712(3)	10.6531(3)	10.585(4)	10.5578(3)
V (Å^3)	1181.3(1)	1209.0(1)	1186(1)	1176.9(1)
size (μm)	70×60×40	70×60×40	80×70×50	95×95×90
θ_{max} (Mo$K\alpha$)	32	32	32	32
R_{int} (%)	5.27	4.25	13.16	4.80
indep. refl.	124	126	129	123
obs. refl. $[F_o > 4\sigma(F_o)]$	108	97	77	109
Ref. param.	12	13	13	12
$R1_{all}$ (%)	3.05	6.27	9.39	3.39
$R1_{obs}$ (%)	2.46	4.09	4.81	2.98
$\Delta\rho_{max}$ (e/Å^3)	0.53	1.04	0.96	0.37
$\Delta\rho_{min}$ (e/Å^3)	–0.58	–1.81	–1.00	–0.94

Table 3. Selected bond distances and structural parameters for the selected crystals.

	L1	**L8**	**L8_2Tl**	**L8_2Tl-W**	**L9**	**L9_Tl**	**L11**	**L14**
n.e$^-$ (A)	4.4	4.2	61.0	22.8	4.2	56.8	4.0	4.2
n.e$^-$ (A′)	2.3	2.5	-	15.5	1.8	-	3.6	3.3
n.e$^-$ (Y′)	9.2	9.1	5.3	11.3	9.1	4.6	9.2	9.0
x_{48f} (X)	0.3126(4)	0.3130(3)	0.3102(9)	0.3114(6)	0.3129(3)	0.3104(8)	0.3137(7)	0.3135(3)
x_{32e} (A′)	0.518(2)	0.5178(16)	-	0.5235(7)	0.519(4)	-	0.516(3)	0.5149(12)
x_{32e} (Y′)	0.392(10)	0.396(4)	0.409(7)	0.436(3)	0.382(10)	0.404(5)	0.401(4)	0.401(2)
A-X (×6)	2.719(3)	2.717(2)	2.761(7)	2.751(5)	2.721(2)	2.761(7)	2.718(6)	2.713(2)
A-Y′ (×2)	2.40(8)	2.44(4)	2.58(7)	2.88(4)	2.34(7)	2.54(5)	2.49(3)	2.49(2)
<A-O>	2.639	2.648	2.716	2.783	2.626	2.706	2.659	2.657
B-X (×6)	1.979(2)	1.981(1)	1.988(3)	1.991(2)	1.983(1)	1.990(3)	1.989(3)	1.983(1)
A′-X (×3)	2.78(3)	2.78(2)	-	2.842(9)	2.79(5)	-	2.78(4)	2.765(13)
(×3)	2.69(3)	2.69(2)	-	2.725(10)	2.69(5)	-	2.69(4)	2.688(13)
A′-Y′(×2)	2.73(11)	2.76(5)	-	3.29(4)	2.68(12)	-	2.78(6)	2.75(3)
<A′-O>	2.73	2.74	-	2.920	2.73	-	2.75	2.732
Y′-X (×3)	3.13(9)	3.09(4)	3.03(6)	2.84(4)	3.23(11)	3.07(4)	3.04(3)	3.04(2)
(×3)	3.49(11)	3.53(5)	3.75(8)	4.09(4)	3.38(11)	3.69(6)	3.59(3)	3.58(3)
<Y′-X>	3.31	3.31	3.39	3.47	3.31	3.38	3.32	3.31
X-X (u.)	2.800(6)	2.807(5)	2.788(14)	2.805(10)	2.809(5)	2.793(13)	2.825(11)	2.814(5)
X-X (s.)	2.798(3)	2.797(2)	2.834(5)	2.827(4)	2.801(2)	2.836(5)	2.801(4)	2.795(2)
<X-X>	2.799	2.802	2.811	2.816	2.805	2.815	2.813	2.805
X-B-X (u.)	90.0(2)	90.2(1)	89.0(4)	89.5(3)	90.1(1)	89.2(3)	90.5(3)	90.4(1)
X-B-X (s.)	90.0(2)	89.8(1)	91.0(4)	90.5(3)	89.9(1)	90.8(3)	89.5(3)	89.6(1)
B-X-B	141.0(2)	140.8(2)	142.4(5)	141.7(4)	140.9(2)	142.3(5)	140.3(4)	140.5(2)
B-X-A	104.06(7)	104.12(5)	103.6(2)	103.8(1)	104.10(5)	103.7(2)	104.2(1)	104.21(5)
A-X-A	86.7(1)	86.78(8)	85.9(3)	86.3(2)	86.74(8)	86.0(3)	87.0(2)	86.94(9)
σ^2 (B)	0.00	0.05	0.97	0.22	0.03	0.81	0.26	0.18

Notes: u. = unshared edge of the octahedron; s. = shared edge between B and A polyhedral. Bond angle variance (σ^2) was computed according to the formula proposed by Robinson et al. (1971).

Table 4. Crystal-chemical formulae for untreated pyrochlore supergroup minerals from Lueshe

L1	$[\square_{1.13}(H_2O)_{0.58}Sr_{0.18}Na_{0.09}Ca_{0.01}Pb_{0.01}]_{\Sigma 2.00}(Nb_{1.83}Ti_{0.17})[O_{4.43}(OH)_{1.57}][(H_2O)_{0.89}K_{0.11}]$	(1)
	$[\square_{1.13}(H_3O)_{0.58}Sr_{0.18}Na_{0.09}Ca_{0.01}Pb_{0.01}]_{\Sigma 2.00}(Nb_{1.83}Ti_{0.17})[O_{5.90}(OH)_{0.10}][(H_3O)_{0.89}K_{0.11}]$	(2)
L11	$[(H_2O)_{0.90}\square_{0.89}Sr_{0.18}Na_{0.01}Ca_{0.01}Pb_{0.01}]_{\Sigma 2.00}(Nb_{1.84}Ti_{0.16})[O_{4.36}(OH)_{1.64}][(H_2O)_{0.89}K_{0.11}]$	(1)
	$[(H_3O)_{0.90}\square_{0.89}Sr_{0.18}Na_{0.01}Ca_{0.01}Pb_{0.01}]_{\Sigma 2.00}(Nb_{1.84}Ti_{0.16})O_6[(H_3O)_{0.74}(H_2O)_{0.15}K_{0.11}]$	(2)
L14	$[\square_{0.92}(H_2O)_{0.83}Sr_{0.18}Na_{0.05}Ca_{0.01}Pb_{0.01}]_{\Sigma 2.00}(Nb_{1.84}Ti_{0.16})[O_{4.38}(OH)_{1.62}][(H_2O)_{0.91}K_{0.09}]$	(1)
	$[\square_{0.92}(H_3O)_{0.83}Sr_{0.18}Na_{0.05}Ca_{0.01}Pb_{0.01}]_{\Sigma 2.00}(Nb_{1.84}Ti_{0.16})O_6[(H_3O)_{0.79}(H_2O)_{0.12}K_{0.09}]$	(2)
L9_Tl	$(Tl_{1.29}\square_{0.53}Sr_{0.17}Na_{0.01})_{\Sigma 2.00}(Nb_{1.83}Ti_{0.17})[O_{5.56}(OH)_{0.44}](\square_{0.91}K_{0.06}Tl_{0.03})$	

Note: Crystal-chemical formulae were obtained assuming that the initial aqueous species in untreated crystals is H_2O (1) or mainly H_3O^+ (2) and for Tl-Imb crystal.

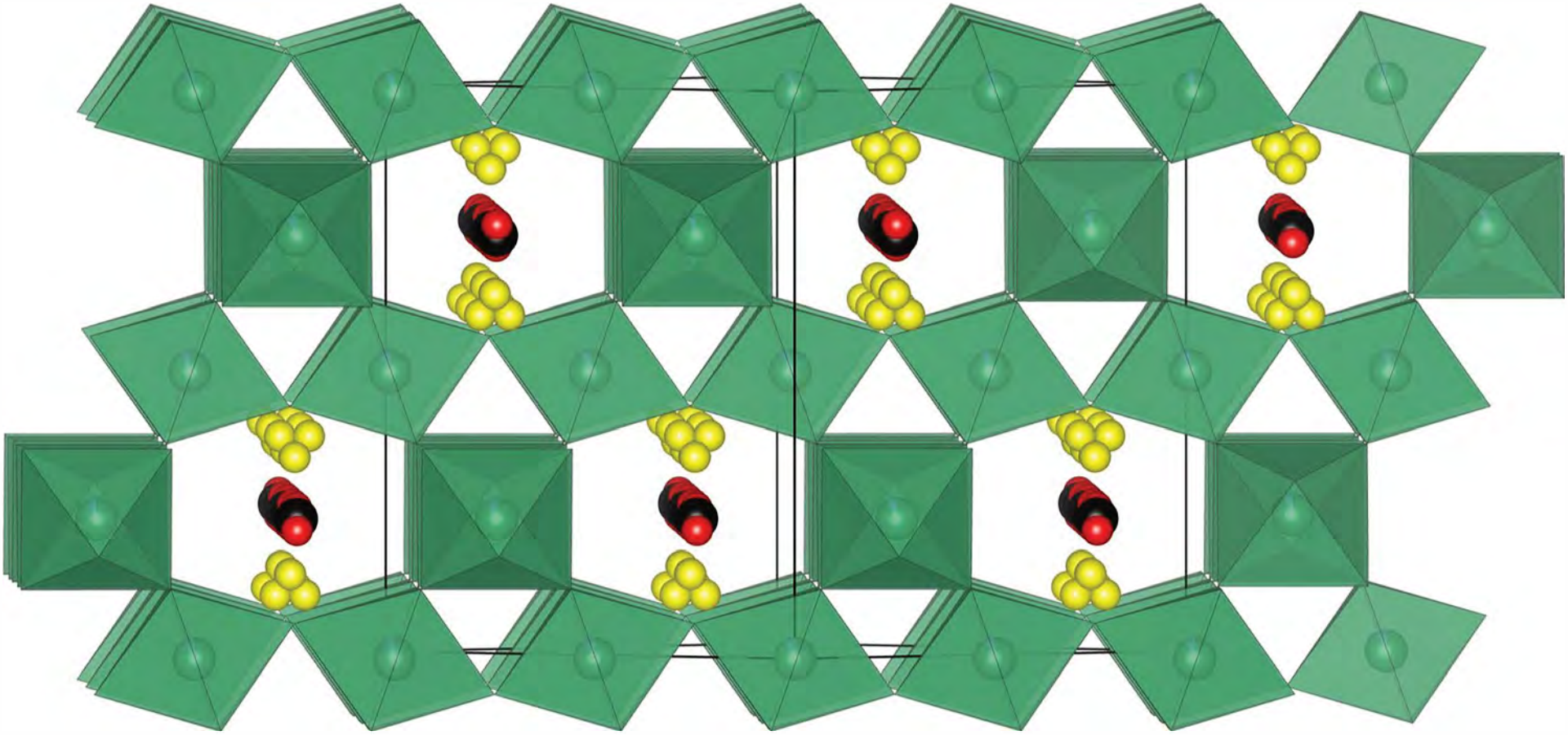

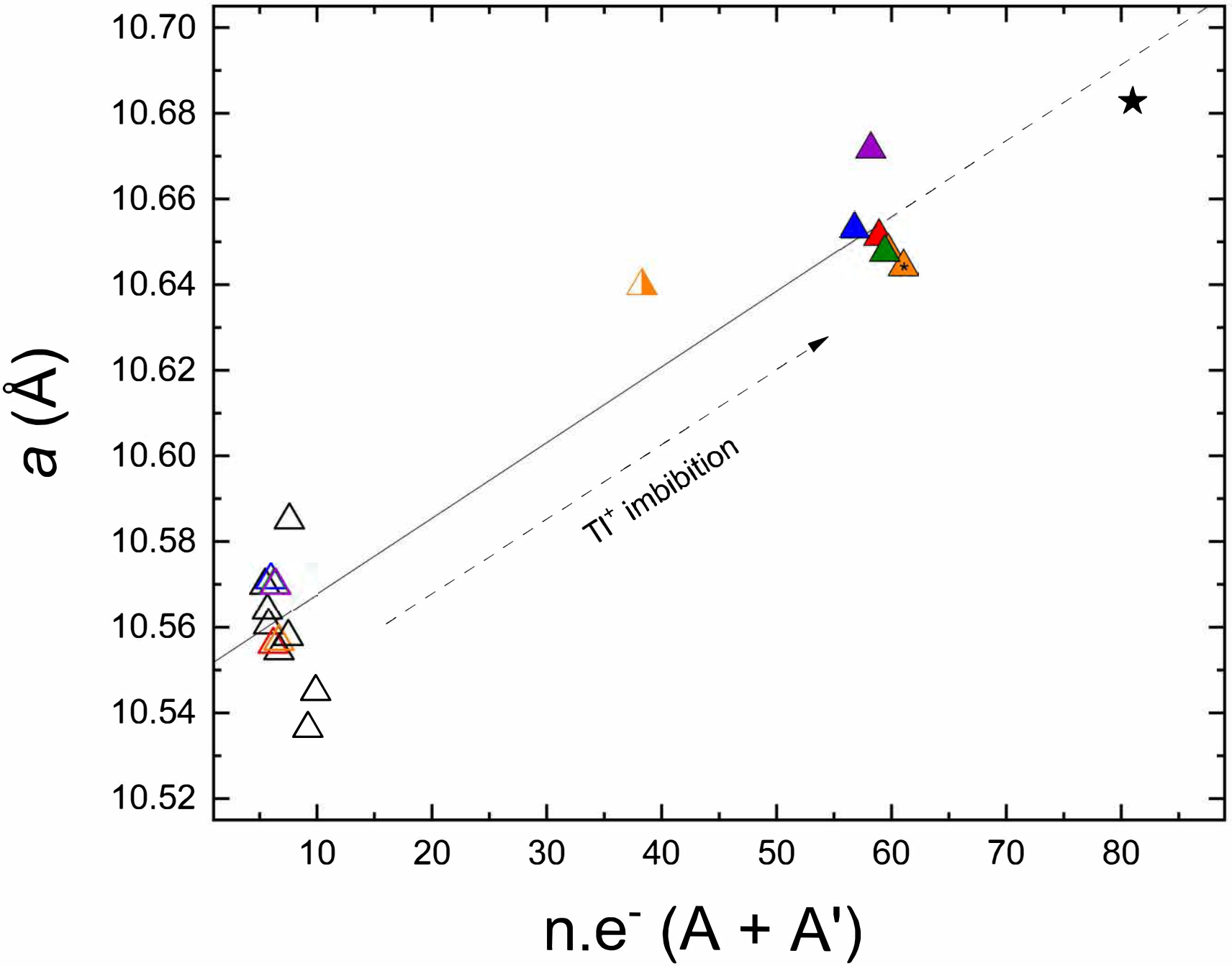
10.70
10.68
10.66
10.64
10.62
10.60
10.58
10.56
10.54
10.52
a (Å)
10
20
30
40
50
60
70
80
n.e⁻ (A + A')
Tl+ imbibition

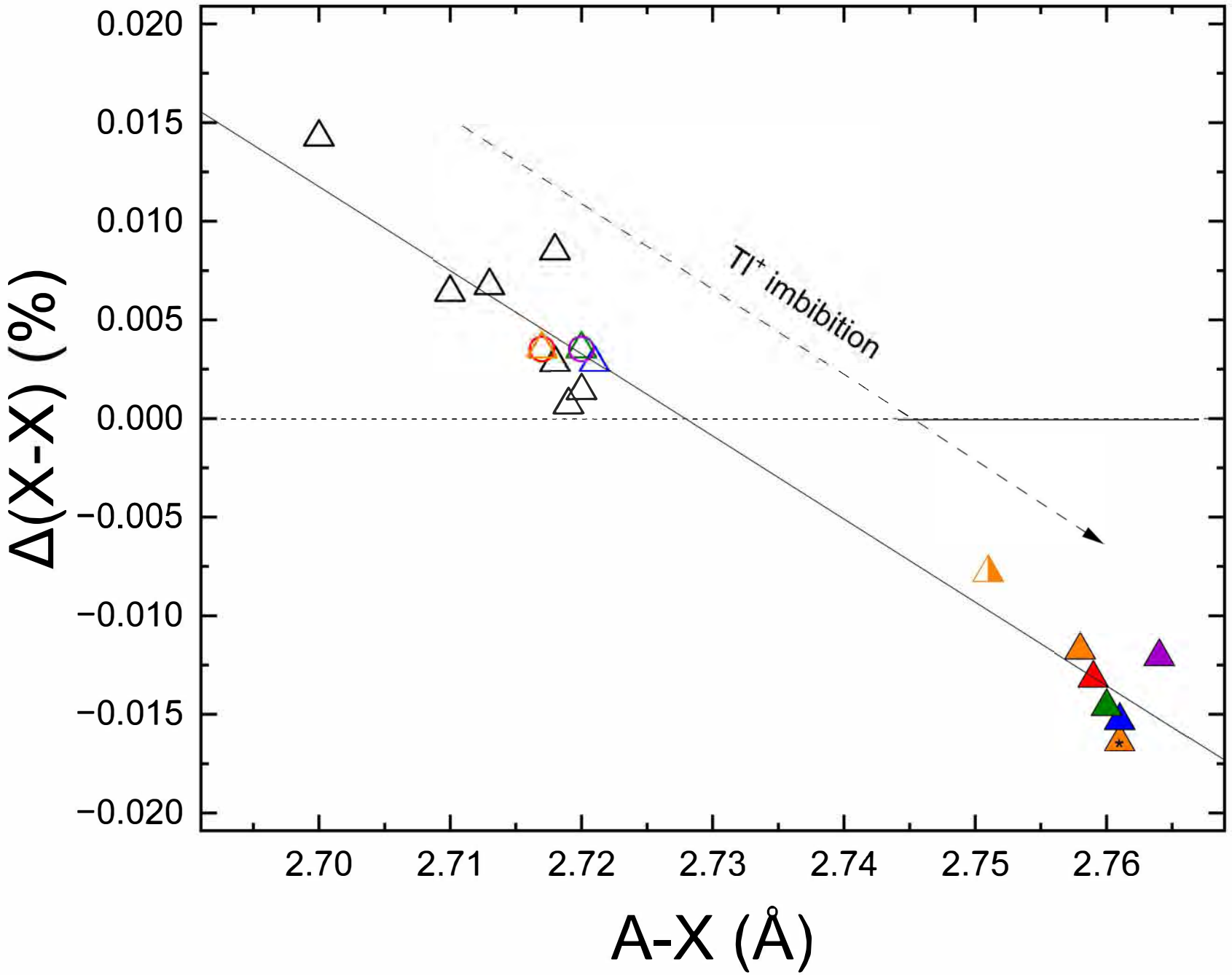
0.020
0.015
0.010
0.005
0.000
−0.005
−0.010
−0.015
−0.020
Δ(X-X) (%)
2.70
2.71
2.72
2.73
2.74
2.75
2.76
A-X (Å)
Tl+ imbibition

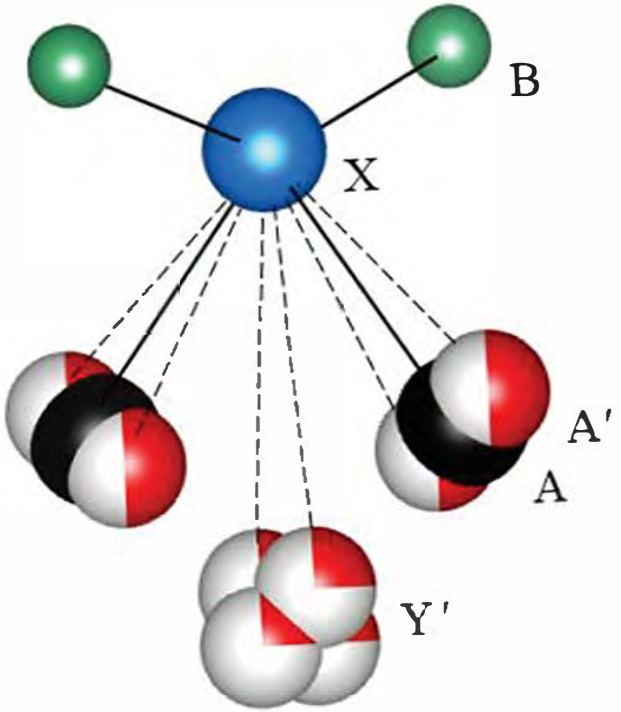
B
X
A'
A
Y'

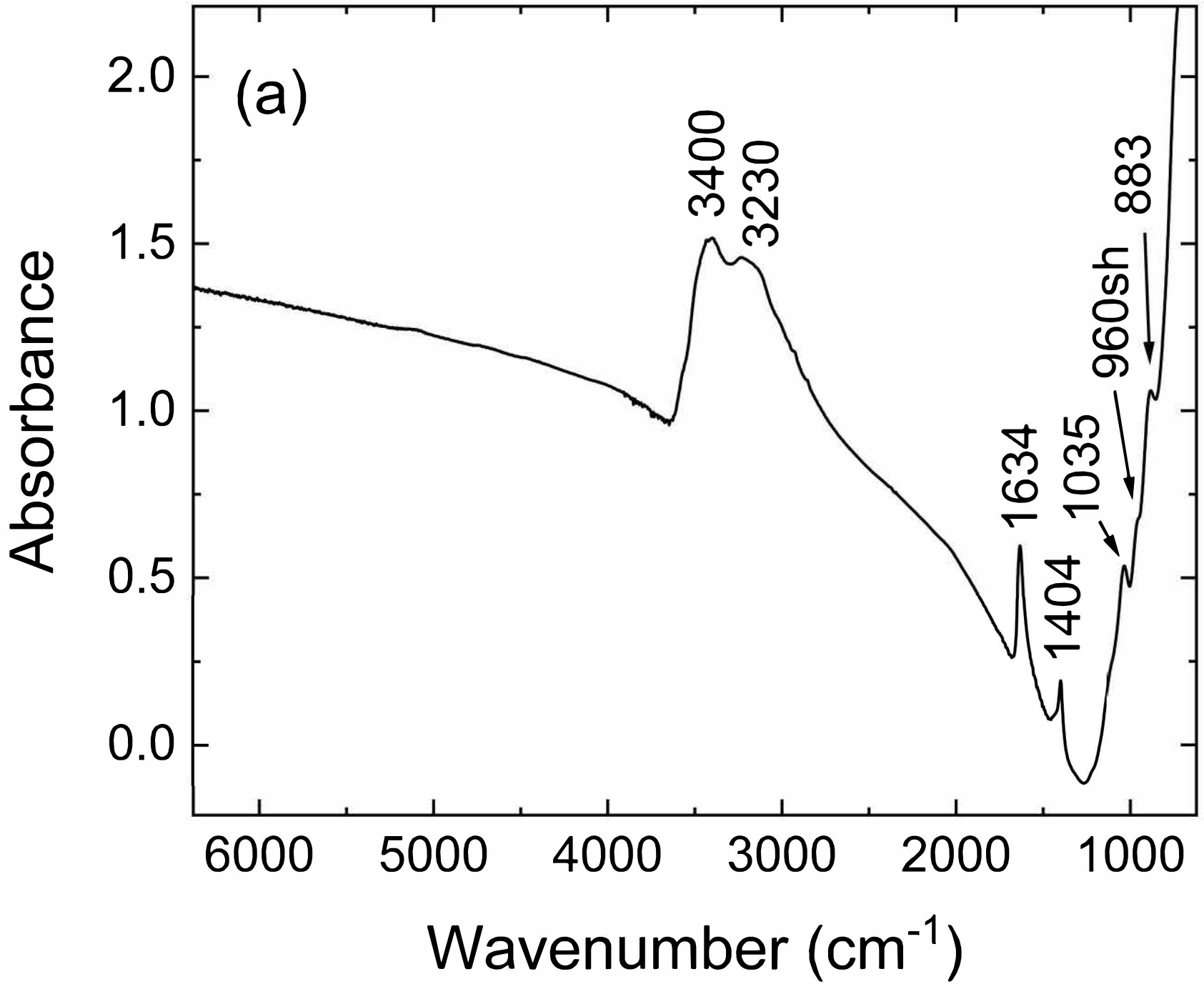
(a)
3400
3230
1634
1404
1035
960sh
883
Absorbance
Wavenumber (cm-1)
2.0
1.5
1.0
0.5
0.0
6000
5000
4000
3000
2000
1000

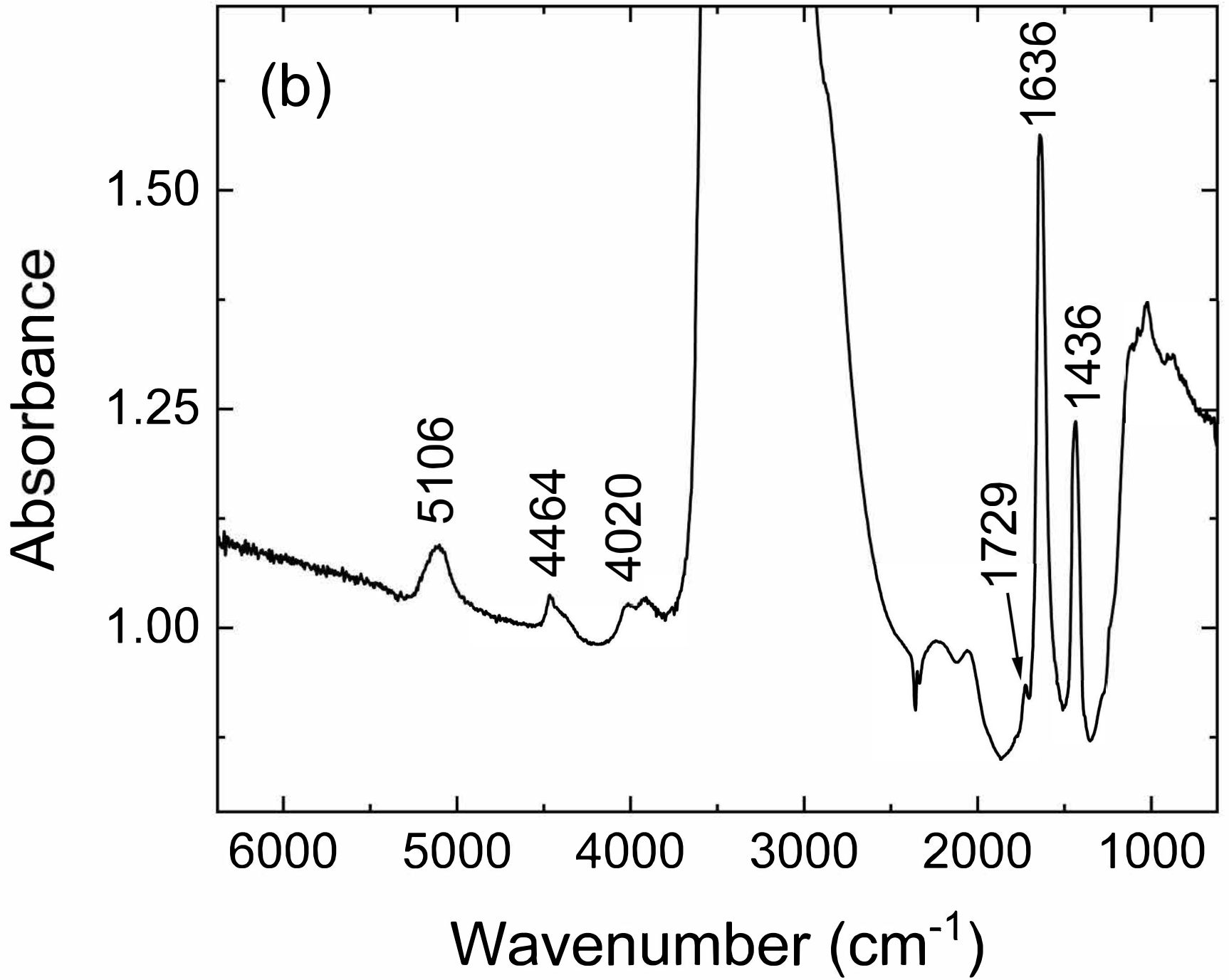
(b)
1.50
1.25
1.00
Absorbance
5106
4464
4020
1729
1636
1436
6000
5000
4000
3000
2000
1000
Wavenumber (cm-1)

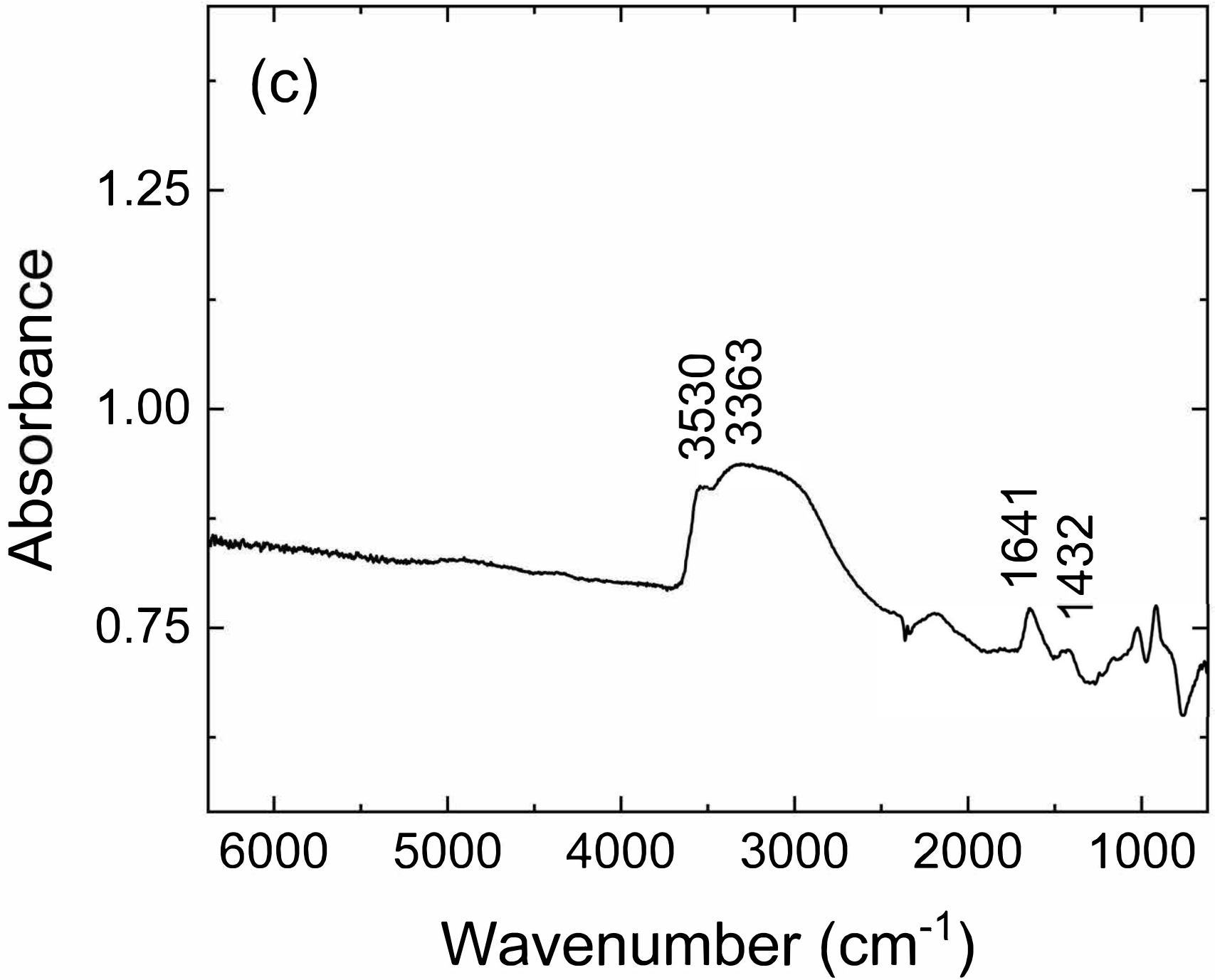
(c)
Absorbance
1.25
1.00
0.75
3530
3363
1641
1432
6000
5000
4000
3000
2000
1000
Wavenumber (cm-1)

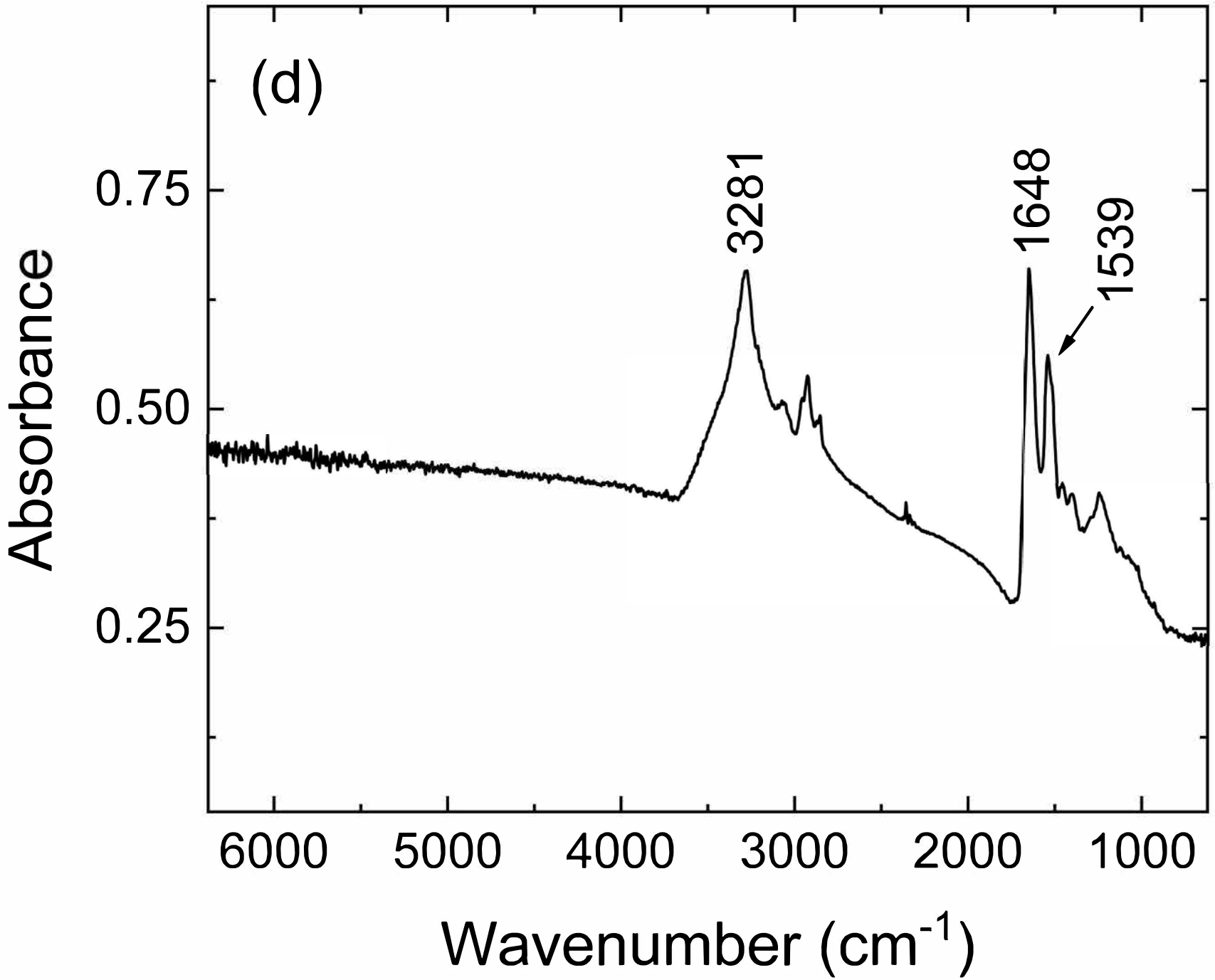
(d)
3281
1648
1539
0.75
0.50
0.25
Absorbance
6000
5000
4000
3000
2000
1000
Wavenumber (cm-1)

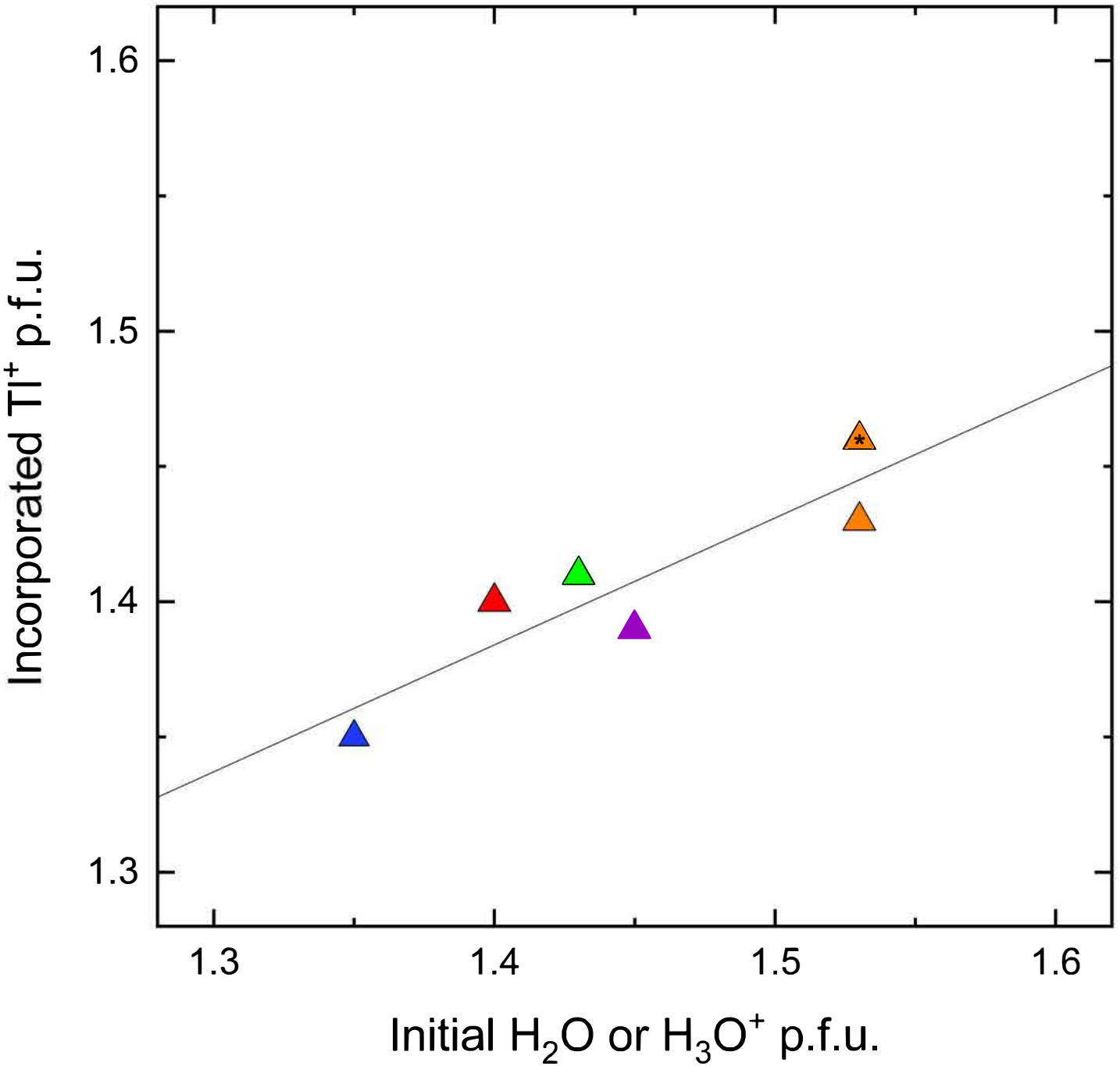
1.6
1.5
1.4
1.3
1.3
1.4
1.5
1.6
Incorporated Tl^+ p.f.u.
Initial H_2O or H_3O^+ p.f.u.
*